GAMM-Mitt. **31**, No. 2, 133 – 150 (2008) / **DOI** 10.1002/gamm.200890007

Thermodynamic consistent modelling of defects and microstructures in ferroelectrics

Ralf Müller[*1], **Jörg Schröder**[2], and **Doru C. Lupascu**[3]

[1] Department of Civil Engineering & Geodesy, Solid Mechanics, Darmstadt University of Technology, Hochschulstr.1, 64289 Darmstadt, Germany
[2] Institute of Mechanics, Faculty of Engineering Science/Division Civil Engineering University Duisburg-Essen, 45117 Essen, Universitätsstr. 15, Germany
[3] Institute for Materials Science, Dresden University of Technology, 01062 Dresden, Germany

Received 22 April 2008, accepted 01 August 2008
Published online 08 December 2008

Key words Ferroelectrics, defects, invariant theory, micromechanics.
MSC (2000) 82D45, 74F15, 74M25

The paper describes the main phenomena associated with fatigue in ferroelectric materials due to defects and microstructural effects. An analysis the modelling on different length scales is presented. Starting from a thermodynamic analysis of the macroscopic material behavior other microscopic aspects are addressed. The introduction of an orientation distribution function allows for a computationally efficient extension of a single crystal model to realistic 3D structures. Additionally, the thermodynamic treatment of defects and domain wall motion is discussed to provide a better understanding of various micro-mechanisms. It is explained by the concept of configurational/driving forces, how defects influence each other and how the mobility of domain walls is reduced in the presence of defects.

1 Introduction

Ferroelectric materials are widely used in sensor and actuator applications. Their atomistic structure allows the materials to couple electric fields with mechanical fields. Another important field of application are non-volatile memories based on ferroelectrics (ferroelectric random access memory, FeRAM). On the macroscopic level a rather complex material behavior is observed. This complex behavior is due to microstructural changes. In polycrystalline ferroelectrics each crystal consists of many domains (regions with almost constant spontaneous polarization). Due to external loads these domain structures change and modify the overall material behavior. In addition to these structural changes defects are present in the material and change their arrangement during loading by external fields and in the presence of internal fields, arising from incompatible and charged microstructures.
The aim of this paper is to address the main features on the macro- and microscopic level together with a discussion of some appropriate modelling approaches for these phenomena.

* Corresponding author: e-mail: r.mueller@mechanik.tu-darmstadt.de, Phone: +00 49 6151 164648, Fax: +00 49 6151 163018

2 Experimental observations

The interaction of ferroelectric domains or domain walls with any type of defect will alter the electric response of the material to external electric or mechanical loads. In the case of isolated point defects this interaction is small and has similarities to the interaction of dislocations with point defects in metals. It essentially generates a friction effect on the domain wall. For extended defects the interaction may become considerably stronger and reach values when it is no longer surpassed by the thermal fluctuation of the domain wall. In this case the motion of the wall becomes partly or entirely disruptive. Acoustic emissions or electrical Barkhausen pulses become detectable reflecting the jump-like motion of domain walls [1–3].

a)  b) 

Fig. 1 (online colour at: www.gamm-mitteilungen.org) Features of a microstructure in a ferroelectric ceramic: a) Scanning electron micrograph of a polished surface of barium titanate ($BaTiO_3$). The topographic features are grain boundaries and domain walls accentuated by a chemical etching step using a HF/HCl mixture. The coloring stems from the birefringence of $BaTiO_3$ under polarized light. Image width is 700μm, b) transmission electron micrograph of a single barium titanate grain exposing microdefects and their interaction with domain walls (image width 6μm, courtesy by H. Gorzawski).

The microstructure of a ferroelectric ceramic is generally complex, see Fig. 1a). At least three scales can be identified amended by the external electrical and mechanical boundary conditions. Point defects like missing atoms, interstitial atoms, ions, or localized electronic states represent the smallest scale. Clusters of point defects beyond a certain size or electrical strength can clamp the domain. If a defect has reached the typical scale (geometrical or in electrical strength) of the domain system like in Fig. 1b) its influence on the domain system is strongest. The grain size represents the third scale in the system. Feature sizes of the domain structure scale with the grain size [4]. At the grain scale defects in or at the grain boundary will influence the dynamics of the domain system. One possibility of interaction stems from the formation of charged grain boundaries which is the typical case for highly non-linear PTCR resistors (positive temperature coefficient resistor) [5]. A mechanism active at the grain boundary is charge rearrangement potentially responsible for aging. Aging is the change of material properties with time. In ferroelectrics the domain mobility decreases with time for acceptor doped (”hard doped”) compositions. Several mechanisms have been claimed to be responsible, one at the scale of point defects [6], another one at the scale of the grain boundary. For the latter, the local charge-up of the grain boundary accounts for a compensation of polarization. The alternately charged grain boundary interface then clamps the domain wall motion electrostatically [7]. The largest scale is that of the sample or device. Beside the mechanical boundaries of the ceramic, the electrodes play a particular role in the system. From a continuum point of view the electrode is a boundary of equal electrical potential. As such,

it is easily represented in modelling as well. In the real world a multitude of electrochemical and quantum mechanical mechanisms influence the structure of the interface and thus the electrical boundary conditions. Clustering of oxygen vacancies [8], charge injection by tunneling [9], and modification of the interface energy by surface states are mechanisms under discussion [11]. Each may alter the dynamics of ferroelectric domains.

The ferroelectric state is characterized by the collective displacement of identical ions in the unit cells of an ionic crystal. This displacement entails a macroscopic electric polarization to which external electric fields can couple. A local dipole is formed. The sum of all local dipoles adds up to the macroscopic polarization. Depending on the crystal structure, one, two, four, or more orientations of polarization are permitted in the crystal. In the perovskite structure found in most technologically relevant materials, six orientations (also called variants) are possible. Strain couples to the polarization via electrostriction and transforms the polarization tensor of rank one to a strain tensor of rank two. As a direct consequence, external mechanical forces can alter the polarization state only indirectly and complete depolarization of an initially electrically poled polycrystalline sample is not possible by mechanical forces. A domain in a ferroelectric crystal or grain is a region of equal orientation of the polarization vector. Their average on the grain level cancels to zero for a statistical occupancy of the different variants in a crystal. An external poling process is needed to generate an effective macroscopic polarized state and a macroscopic electromechanical coupling.

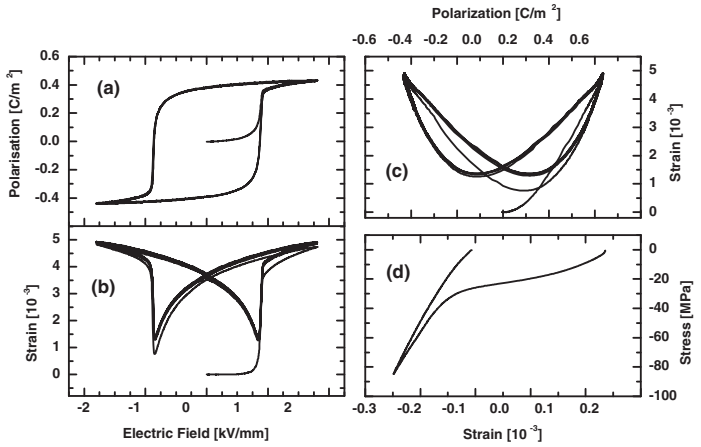

Fig. 2 Electrical and mechanical hysteresis of a commercial ferroelectric ceramic lead zirconate titanate: (a) Electrical hysteresis, (b) resulting longitudinal strain response under electrical drive, (c) macroscopically effective electrostrictive coupling strain vs. polarization, and (d) stress-strain response of a polarized lead lanthanum zirconate titanate (data in (d) C. S. Lynch [14]).

Fig. 2 displays the macroscopic hystereses of a commercial lead zirconate titanate solid solution ceramic material (PIC 151). These types of hysteresis are the result of the rearrangement of the domain structure during poling and subsequent electric polarization reversal. For a

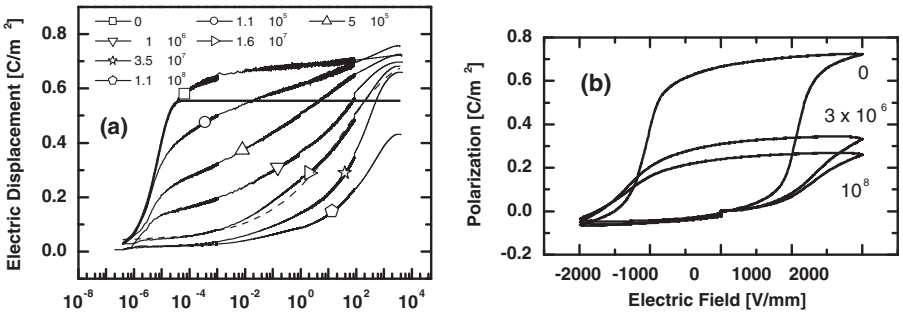

Fig. 3 Effects of bipolar material fatigue: (a) Reduced switching dynamics of the domain system [16], (b) reduced polarization amplitude of the electrical hysteresis.

macroscopic sample electrostriction, which is the quadratic relation between strain and polarization, is not strictly valid due to features of the microstructure: Fig. 2c). Mechanical compressive stress along the poling direction yields the stress strain hysteresis: Fig. 2d). Further details and many references are found in Refs. [12, 13].
Fatigue induces a strong alteration of the electrical and mechanical defect arrangement within the microstructure. These in turn alter many facets of domain dynamics. The most relevant one is the time delay in domain response (Fig. 3a)) changing by many orders of magnitude. This delay entails the reduction of the electrical and mechanical hysteresis (Fig. 3b)) which is measured at a certain rate and thus reflects a certain range of material time constants. If measured very slowly, also fatigued samples show very little modifications of their hysteresis. On top of the time delay, asymmetries in the macroscopic response reflect a certain anisotropic rearrangement of charged defects the very nature of which still has not been determined [15].

Modelling material response in ferroelectrics is thus a multi-scale problem of many facets. A first step is tackled by modelling the influence of extended microscopic defects on domain walls.

3 Thermodynamic preliminaries

Let $\mathcal{B} \subset \mathbb{R}^3$ be the macroscopic body of interest which is parameterized in $\overline{\boldsymbol{x}}$. Furthermore, let $\overline{\boldsymbol{u}}$ be the macroscopic displacement field. The basic kinematic variable is the macroscopic strain tensor $\overline{\boldsymbol{\varepsilon}}$, which is defined by the symmetric part of the macroscopic displacement gradient. As the basic electric field variable we choose the macroscopic electric field vector $\overline{\boldsymbol{E}}$, given by the negative gradient of the macroscopic scalar potential $\overline{\varphi}$. Thus the basic macroscopic quantities are

$$\overline{\boldsymbol{\varepsilon}}(\overline{\boldsymbol{x}}) := \mathrm{sym}[\overline{\nabla}\overline{\boldsymbol{u}}(\overline{\boldsymbol{x}})] \quad \text{and} \quad \overline{\boldsymbol{E}}(\overline{\boldsymbol{x}}) := -\overline{\nabla}\,\overline{\varphi}(\overline{\boldsymbol{x}}) \,, \tag{1}$$

where $\overline{\nabla}$ denotes the gradient operator with respect to $\overline{\boldsymbol{x}}$. The governing field equations from the macroscopic point of view are the balance of momentum and Gauß' law representing the mechanical equilibrium equation and one of the Maxwell equations for the quasi static case

$$\mathrm{div}\overline{\boldsymbol{\sigma}} + \overline{\boldsymbol{f}} = \boldsymbol{0} \quad \text{and} \quad \mathrm{div}\overline{\boldsymbol{D}} = \overline{q} \,. \tag{2}$$

Here $\overline{\boldsymbol{\sigma}}$ represents the macroscopic symmetric Cauchy stress tensor, $\overline{\boldsymbol{f}}$ the given body force, $\overline{\boldsymbol{D}}$ the vector of macroscopic electric displacements and $\overline{q}$ is the given density of free charge carriers. In order to treat the electromechanical boundary value problem, the surface of the considered body is divided into mechanical and electrical parts $\partial\mathcal{B} = \partial\mathcal{B}_u \cup \partial\mathcal{B}_\sigma$ and $\partial\mathcal{B} = \partial\mathcal{B}_\varphi \cup \partial\mathcal{B}_\mathcal{D}$, respectively, with $\partial\mathcal{B}_u \cap \partial\mathcal{B}_\sigma = \emptyset$ and $\partial\mathcal{B}_\varphi \cap \partial\mathcal{B}_D = \emptyset$. The essential boundary conditions on $\partial\mathcal{B}_u$ and $\partial\mathcal{B}_\varphi$ as well as the natural boundary conditions on $\partial\mathcal{B}_\sigma$ and $\partial\mathcal{B}_D$ are $\overline{\boldsymbol{u}} = \overline{\boldsymbol{u}}_b$ on $\partial\mathcal{B}_u$, $\overline{\varphi} = \overline{\varphi}_b$ on $\partial\mathcal{B}_\varphi$, $\overline{\boldsymbol{t}} = \overline{\boldsymbol{\sigma}}\,\overline{\boldsymbol{n}}$ on $\partial\mathcal{B}_t$ and $\overline{Q} = -\overline{\boldsymbol{D}} \cdot \overline{\boldsymbol{n}}$ on $\partial\mathcal{B}_D$.
In the proposed two-scale homogenization approach we do not specify any explicit constitutive relations for the dependent macroscopic quantities $\boldsymbol{\sigma}, \boldsymbol{D}$ in terms of the basic field variables $\overline{\boldsymbol{\varepsilon}}$ and $\overline{\boldsymbol{E}}$. In fact, the dependent macroscopic quantities have to be defined as expedient expectation values of the mesoscopic counterparts $\overline{\boldsymbol{\sigma}}$ and $\overline{\boldsymbol{D}}$. Here we assume the existence of a representative volume element $(\mathcal{RVE})$ associated to each macroscopic material point $\overline{\boldsymbol{x}}$, see Fig. 4. The $\mathcal{RVE} \subset \mathbb{R}^3$ is parameterized in the mesoscopic coordinates $\boldsymbol{x}$. For ferroelectric materials we observe on the meso-scale areas of equal polarization, the individual domains, separated by the domain walls.

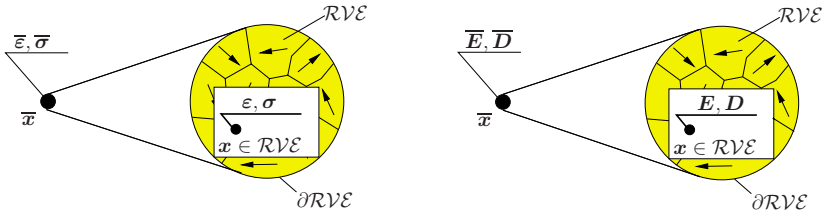

Fig. 4 (online colour at: www.gamm-mitteilungen.org) Mesoscopic mechanical and electrical variables on a representative volume element $(\mathcal{RVE})$.

On the meso-scale the basic variables are the displacement field $\boldsymbol{u}$ and the electric potential φ. Similar to the approach on the macro-scale we define the mesoscopic strain tensor and the mesoscopic electric field vector by

$$\boldsymbol{\varepsilon} := \mathrm{sym}[\nabla \boldsymbol{u}(\boldsymbol{x})] \quad \text{and} \quad \boldsymbol{E} := -\nabla\,\varphi(\boldsymbol{x})\,, \tag{3}$$

respectively. The balance laws of interest are the balance of momentum and Gauß' law

$$\mathrm{div}\boldsymbol{\sigma} = \boldsymbol{0} \quad \text{and} \quad \mathrm{div}\boldsymbol{D} = 0\,, \tag{4}$$

respectively, neglecting body forces and free charge carriers. Furthermore, the macroscopic quantities are defined through surface integrals over the boundary of the representative volume element $\partial\mathcal{RVE}$:

$$\begin{aligned} \overline{\boldsymbol{\varepsilon}} &:= \frac{1}{V}\int_{\partial\mathcal{RVE}} \mathrm{sym}[\boldsymbol{u} \otimes \boldsymbol{n}]\; dA\,, & \overline{\boldsymbol{\sigma}} &:= \frac{1}{V}\int_{\partial\mathcal{RVE}} \mathrm{sym}[\boldsymbol{t} \otimes \boldsymbol{x}]\; dA\,, \\ \overline{\boldsymbol{E}} &:= \frac{1}{V}\int_{\partial\mathcal{RVE}} -\varphi\,\boldsymbol{n}\; dA\,, & \overline{\boldsymbol{D}} &:= -\frac{1}{V}\int_{\partial\mathcal{RVE}} Q\,\boldsymbol{x}\; dA\,. \end{aligned} \tag{5}$$

4 Approximation of Microstructures via discrete ODF

In the last section we have defined the relation between the macroscopic and microscopic variables. In order to derive different constraint/boundary conditions for the considered body on the meso-scale, the representative volume element, we postulate a generalized macro-homogeneity condition which equates the mesoscopic and macroscopic electromechanical power, in this context see the well known Hill condition [19]. In the following we assume a decoupling of the mechanical and electrical contributions and focus on continuous bodies without holes. The two decoupled macro-homogeneity conditions are defined as

$$\mathcal{P}_1 := \frac{1}{V}\int_{\mathcal{RVE}} \boldsymbol{\sigma} : \dot{\varepsilon}\, dV - \overline{\boldsymbol{\sigma}} : \dot{\overline{\varepsilon}} \quad \text{and} \quad \mathcal{P}_2 := \frac{1}{V}\int_{\mathcal{RVE}} \boldsymbol{D}\cdot\dot{\boldsymbol{E}}\, dV - \overline{\boldsymbol{D}}\cdot\dot{\overline{\boldsymbol{E}}}\,. \tag{6}$$

Simple conditions, here denoted as constraints on the meso-structure, satisfying Eq. (6) are

$$\boldsymbol{\sigma} = \overline{\boldsymbol{\sigma}} \quad \text{or} \quad \dot{\varepsilon} = \dot{\overline{\varepsilon}} \quad \text{and} \quad \boldsymbol{D} = \overline{\boldsymbol{D}} \quad \text{or} \quad \dot{\boldsymbol{E}} = \dot{\overline{\boldsymbol{E}}}\,. \tag{7}$$

In this contribution the microstructure is approximated by an orientation distribution function (ODF) of the anisotropy axis of the considered transversely isotropic material. A feasible access for the construction of uniformly distributed preferred directions is the partitioning of the sphere surface into parts of equal areas. An innovative treatment of the problem was given by RICHARD BUCKMINSTER FULLER who separated the surface of the sphere into equilateral congruent triangles. The resulting constructions of a dome are denoted by the expressions geodesic spheres or geodesic domes. They were presented to a wider audience during the world exhibition 1967 in Montreal where the American pavillon was constructed in the mentioned manner.

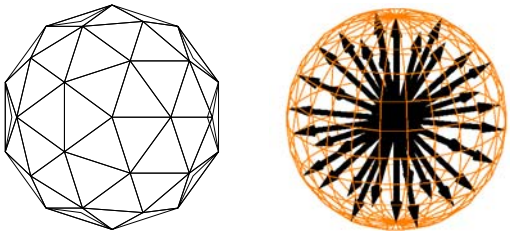

Fig. 5 (online colour at: www.gamm-mitteilungen.org) Geodesic spheres and their distribution of orientations for 42 orientations.

We use this consistent segmentation of the unit sphere and assign one preferred direction to each node of the triangles. Fig. 5 shows two geodesic spheres for the frequency and the corresponding distribution of preferred directions. The geodesic sphere is constructed by 42 nodal points and consequently we get 42 preferred directions. Further details are discussed in [30] and [27].

For the explicit formulation of coordinate-invariant transversely isotropic constitutive equations the representation theory of isotropic tensor functions is used. The governing equations represent automatically the material symmetries of the body of interest, i.e. the enthalpy function has to be invariant under all transformations $\boldsymbol{Q} \in \mathcal{G}_{ti}$, see [23] and [34], page 250-251:

$$\hat{H}(\varepsilon, \boldsymbol{E}, \boldsymbol{\xi}) = \hat{H}(\boldsymbol{Q}\varepsilon\boldsymbol{Q}^T, \boldsymbol{Q}\boldsymbol{E}, \boldsymbol{Q}*\boldsymbol{\xi}) \quad \forall \quad \boldsymbol{Q} \in \mathcal{G}_{ti} = \{\boldsymbol{Q} \in \mathcal{O}(3),\ \boldsymbol{Q}\boldsymbol{a} = \boldsymbol{a}\}\,, \tag{8}$$

here $\boldsymbol{\xi}$ denotes the set of internal vector- and tensor-valued internal variables and $(\boldsymbol{Q} * \boldsymbol{\xi})$ is an abbreviation of the transformations of the elements of the set. Let $\boldsymbol{\xi} = \boldsymbol{T}, \boldsymbol{v}$, then the transformations are defined through $\boldsymbol{Q} * \boldsymbol{T} = \boldsymbol{Q}\boldsymbol{T}\boldsymbol{Q}^T$ and $\boldsymbol{Q} * \boldsymbol{v} = \boldsymbol{Q}\boldsymbol{v}$ for a second-order tensor $\boldsymbol{T}$ and a vector $\boldsymbol{v}$.

The main idea of a coordinate-invariant representation is the extension of the $\mathcal{G}_{ti}$-invariant functions (8) to functions which are invariant under a larger group of transformations, particularly under all elements of the orthogonal group $\mathcal{O}(3)$. For the invariant formulation of the thermodynamic potential we introduce an additional tensor, the preferred direction $\boldsymbol{a}$, which can be interpreted as a first-order structural tensor. With the principle of isotropy of space, see e.g. [18], we arrive at the representation for the thermodynamic potential:

$$\hat{H}(\boldsymbol{\varepsilon}, \boldsymbol{E}, \boldsymbol{\xi}, \boldsymbol{a}) = \hat{H}(\boldsymbol{Q}\boldsymbol{\varepsilon}\boldsymbol{Q}^T, \boldsymbol{Q}\boldsymbol{E}, \boldsymbol{Q} * \boldsymbol{\xi}, \boldsymbol{Q}\boldsymbol{a}) \quad \forall \quad \boldsymbol{Q} \in \mathcal{O}(3) \; . \tag{9}$$

Eq. (9) is the definition of an isotropic tensor function, i.e. this relationship represents a set of isotropic functions with respect to the whole set of arguments $\{\boldsymbol{\varepsilon}, \boldsymbol{E}, \boldsymbol{\xi}, \boldsymbol{a}\}$. On the other hand Eq. (9) can be interpreted as an anisotropic function with respect to the arguments $\{\boldsymbol{\varepsilon}, \boldsymbol{E}, \boldsymbol{\xi}\}$, i.e. $\hat{H}(\boldsymbol{\varepsilon}, \boldsymbol{E}, \boldsymbol{\xi}, \boldsymbol{a}) = \hat{H}(\boldsymbol{Q}\boldsymbol{\varepsilon}\boldsymbol{Q}^T, \boldsymbol{Q}\boldsymbol{E}, \boldsymbol{Q} * \boldsymbol{\xi}, \boldsymbol{a})$ where this condition holds only and only if $\boldsymbol{Q} \in \mathcal{G}_{ti}$. Due to this observation we conclude that the invariance group of the structural tensor, here the preferred direction $\boldsymbol{a}$, characterizes the type of anisotropy.

4.1 Constitutive Framework

One of the basic assumptions in the proposed model is the often used additive decomposition of the strain tensor $\boldsymbol{\varepsilon}$ and the vector of electric displacements $\boldsymbol{D}$ into their reversible $\{\boldsymbol{\varepsilon}^e, \boldsymbol{D}^e\}$ and remanent parts $\{\boldsymbol{\varepsilon}^r, \boldsymbol{P}^r\}$:

$$\boldsymbol{\varepsilon} = \boldsymbol{\varepsilon}^e + \boldsymbol{\varepsilon}^r \quad \text{and} \quad \boldsymbol{D} = \boldsymbol{D}^e + \boldsymbol{P}^r \; . \tag{10}$$

Consequently, we choose for the set of internal variables in (9) the remanent quantities, i.e.

$$\boldsymbol{\xi} := \{\boldsymbol{\varepsilon}^r, \boldsymbol{P}^r\} \; \rightarrow \; \boldsymbol{Q} * \boldsymbol{\xi} = \{\boldsymbol{Q}\boldsymbol{\varepsilon}^r\boldsymbol{Q}^T, \boldsymbol{Q}\boldsymbol{P}^r\} \; . \tag{11}$$

The observable variables are the total strains $\boldsymbol{\varepsilon}$ and the electric field $\boldsymbol{E}$, whereas the remanent quantities describe the internal state of the material and $\boldsymbol{a}$ reflects the internal orientation of the polarized material. Neglecting thermal effects the second law of thermodynamics yields

$$\mathcal{D} = \boldsymbol{\sigma} : \dot{\boldsymbol{\varepsilon}} - \boldsymbol{D} \cdot \dot{\boldsymbol{E}} - \dot{H} \geq 0 \; . \tag{12}$$

The evaluation of the dissipation inequality leads to the expression

$$\mathcal{D} = (\boldsymbol{\sigma} - \partial_{\boldsymbol{\varepsilon}} H) : \dot{\boldsymbol{\varepsilon}} - (\boldsymbol{D} + \partial_{\boldsymbol{E}} H) \cdot \dot{\boldsymbol{E}} - \partial_{\boldsymbol{\varepsilon}^r} H : \dot{\boldsymbol{\varepsilon}}^r - \partial_{\boldsymbol{P}^r} H \cdot \dot{\boldsymbol{P}}^r \geq 0 \; . \tag{13}$$

This inequality has to be fulfilled for all possible thermodynamic processes, thus we obtain the following constitutive equations for the stresses and electric displacements

$$\boldsymbol{\sigma} = \partial_{\boldsymbol{\varepsilon}} H \quad \text{and} \quad \boldsymbol{D} = -\partial_{\boldsymbol{E}} H \; , \tag{14}$$

respectively. For the thermodynamic forces associated to the remanent quantities we introduce the abbreviations

$$\tilde{\boldsymbol{\sigma}} := -\partial_{\boldsymbol{\varepsilon}^r} H \quad \text{and} \quad \tilde{\boldsymbol{E}} := -\partial_{\boldsymbol{P}^r} H \; , \tag{15}$$

which lead to the reduced dissipation inequality

$$\mathcal{D} = \tilde{\boldsymbol{\sigma}} : \dot{\boldsymbol{\varepsilon}}^r + \tilde{\boldsymbol{E}} \cdot \dot{\boldsymbol{P}}^r \geq 0 \ . \tag{16}$$

Hilbert's Theorem postulates that for a finite set of vectors and tensors an integrity basis consisting of a finite number of invariants exists, see [18] and the references therein. In order to formulate the electric enthalpy function we need this finite set of invariants, which builds the polynomial basis. For detailed representations of scalar- and tensor-valued functions we refer to [32–37], in the context of electromechanically coupled systems see [31]. The finite set of vectors and tensors is given by the symmetric tensors $\boldsymbol{\varepsilon}, \boldsymbol{\varepsilon}^r$, the vectors $\boldsymbol{E}$, $\boldsymbol{P}^r$ and the preferred direction $\boldsymbol{a}$ with $||\boldsymbol{a}|| = 1$. With the normalization condition for $\boldsymbol{a}$, which induces $\text{trace}[(\boldsymbol{a} \otimes \boldsymbol{a})^n] = 1$ for $n = 1, 2, 3$, the basic and mixed invariants of interest in the proposed model are

$$\begin{aligned} &I_1 := \text{trace}[\boldsymbol{\varepsilon} - \boldsymbol{\varepsilon}^r], \quad I_2 := \text{trace}[(\boldsymbol{\varepsilon} - \boldsymbol{\varepsilon}^r)^2], \quad I_4 := \text{trace}[(\boldsymbol{\varepsilon} - \boldsymbol{\varepsilon}^r)(\boldsymbol{a} \otimes \boldsymbol{a})], \\ &I_5 := \text{trace}[(\boldsymbol{\varepsilon} - \boldsymbol{\varepsilon}^r)^2(\boldsymbol{a} \otimes \boldsymbol{a})], \quad J_1 := \text{trace}[(\boldsymbol{E} \otimes \boldsymbol{E})], \quad J_2 := \text{trace}[(\boldsymbol{E} \otimes \boldsymbol{a})], \\ &K_1 := \text{trace}[(\boldsymbol{\varepsilon} - \boldsymbol{\varepsilon}^r)(\boldsymbol{E} \otimes \boldsymbol{a})], \quad \bar{N}^P := \boldsymbol{P}^r \cdot \boldsymbol{a} \ . \end{aligned} \tag{17}$$

The enthalpy function H is formulated in terms of the elements of the polynomial basis

$$H = H(I_1, I_2, I_4, I_5, J_1, J_2, K_1, \bar{N}^P) =: H(L_i | i = 1, ...8) \ , \tag{18}$$

which is invariant under all transformations $\boldsymbol{Q} \in \mathcal{O}(3)$. Of course, polynomial functions in elements of the polynomial basis are also invariant under these transformations. In the above discussed framework we now construct a specific model problem. In this model the underlying thermodynamic potential is divided into five parts and given by

$$H = H_1(\boldsymbol{\varepsilon}, \boldsymbol{\varepsilon}^r) + H_2(\boldsymbol{E}) + H_3(\boldsymbol{\varepsilon}, \boldsymbol{\varepsilon}^r, \boldsymbol{E}, \bar{N}^P) + H_4(\boldsymbol{E}, \bar{N}^P) + H_5(\bar{N}^P) \ . \tag{19}$$

The mechanical, electrical and piezoelectric parts are

$$\begin{aligned} H_1 &= \frac{1}{2}\lambda I_1^2 + \mu I_2 + \alpha_1 I_5 + \alpha_2 I_4^2 + \alpha_3 I_1 I_4 \ , \\ H_2 &= \gamma_1 J_1 + \gamma_2 J_2^2 \ , \\ H_3 &= [\beta_1 I_1 J_2 + \beta_2 I_4 J_2 + \beta_3 K_1] \frac{1}{P_s} \bar{N}^P =: \omega \, \bar{N}^P \ , \end{aligned} \tag{20}$$

respectively. All appearing material properties can be identified from the classical moduli representations. The terms H_4 and H_5 with

$$H_4 = -J_2 \, \bar{N}^P \quad \text{and} \quad H_5 = f(\bar{N}^P) \tag{21}$$

take into account the remanent polarization of the material, where the function $f(\bar{N}^P)$ governs the form of the dielectric hysteresis curve, we choose

$$f(\bar{N}^P) = \frac{1}{c}[\bar{N}^P \text{Artanh}(\frac{\bar{N}^P}{P_s}) + \frac{1}{2} P_s \ln(1 - (\frac{\bar{N}^P}{P_s})^2)] \ . \tag{22}$$

The explicit form of the stresses and electric displacements appear with

$$\boldsymbol{\sigma} = \partial_{\boldsymbol{\varepsilon}} \hat{H} = \sum_{i=1}^{8} \frac{\partial \hat{H}}{\partial L_i} \frac{\partial L_i}{\partial \boldsymbol{\varepsilon}} \quad \text{and} \quad \boldsymbol{D} = -\partial_{\boldsymbol{E}} \hat{H} = -\sum_{i=1}^{8} \frac{\partial \hat{H}}{\partial L_i} \frac{\partial L_i}{\partial \boldsymbol{E}} \tag{23}$$

for the specific model problem (15) as follows

$$\begin{aligned} \boldsymbol{\sigma} &= (\lambda I_1 + \alpha_3 I_4)\mathbf{1} + 2\mu(\boldsymbol{\varepsilon} - \boldsymbol{\varepsilon}^r) + \alpha_1[\boldsymbol{a} \otimes (\boldsymbol{\varepsilon} - \boldsymbol{\varepsilon}^r)\boldsymbol{a} + \boldsymbol{a}(\boldsymbol{\varepsilon} - \boldsymbol{\varepsilon}^r) \otimes \boldsymbol{a}] \\ &+ (2\alpha_2 I_4 + \alpha_3 I_1)\boldsymbol{a} \otimes \boldsymbol{a} + [\beta_1 J_2 \mathbf{1} + \beta_2 J_2 \boldsymbol{a} \otimes \boldsymbol{a} \\ &+ \frac{1}{2}\beta_3(\boldsymbol{E} \otimes \boldsymbol{a} + \boldsymbol{a} \otimes \boldsymbol{E})]\frac{1}{P_s}\bar{N}^P \,, \\ \boldsymbol{D} &= -2\gamma_1 \boldsymbol{E} - 2\gamma_2 J_2 \boldsymbol{a} - [(\beta_1 I_1 + \beta_2 I_4)\boldsymbol{a} + \beta_3 \boldsymbol{a}(\boldsymbol{\varepsilon} - \boldsymbol{\varepsilon}^r)]\frac{1}{P_s}\bar{N}^P + \boldsymbol{P}^r \,. \end{aligned} \tag{24}$$

Here $\boldsymbol{P}^r = -\partial H_4 / \partial \boldsymbol{E} = \bar{N}^P \boldsymbol{a}$ is the remanent polarization wrt. the polarization axis.

4.2 Switching Surface and Remanent Quantities

In order to describe the evolution of the remanent variables the existence of a dissipation potential is assumed. This is expressed as a continuous, convex scalar-valued function of the flux variables $\dot{\boldsymbol{\varepsilon}}^r$ and $\dot{\boldsymbol{P}}^r$, in this context see e.g. [22], [21] and [25]. Applying a Legendre-Fenchel transformation leads to a corresponding potential that can be formulated in terms of the dual quantities. Let us now introduce a switching surface Φ in terms of the dual variables $\tilde{\boldsymbol{\sigma}}$ and $\tilde{\boldsymbol{E}}$, with

$$\Phi(\tilde{\boldsymbol{\sigma}}, \tilde{\boldsymbol{E}}) \leq 0 \,. \tag{25}$$

Applying the principle of maximum remanent dissipation, a generalization of the principle of maximum dissipation, we construct the Lagrangian functional

$$\mathcal{L}(\tilde{\boldsymbol{\sigma}}, \tilde{\boldsymbol{E}}, \lambda) = -\mathcal{D}(\tilde{\boldsymbol{\sigma}}, \tilde{\boldsymbol{E}}) + \lambda \Phi(\tilde{\boldsymbol{\sigma}}, \tilde{\boldsymbol{E}}) \,, \tag{26}$$

with the Lagrange multiplier λ. The optimization conditions, see e.g. [24],

$$\partial_{\tilde{\boldsymbol{\sigma}}} \mathcal{L} = 0 \,, \quad \partial_{\tilde{\boldsymbol{E}}} \mathcal{L} = 0 \,, \quad \partial_{\lambda} \mathcal{L} = 0 \,, \tag{27}$$

lead to the associated flow rules of the remanent variables

$$\dot{\boldsymbol{\varepsilon}}^r = \lambda \partial_{\tilde{\boldsymbol{\sigma}}} \Phi(\tilde{\boldsymbol{\sigma}}, \tilde{\boldsymbol{E}}) \quad \text{and} \quad \dot{\boldsymbol{P}}^r = \lambda \partial_{\tilde{\boldsymbol{E}}} \Phi(\tilde{\boldsymbol{\sigma}}, \tilde{\boldsymbol{E}}) \tag{28}$$

and the loading/unloading conditions $\lambda \geq 0$, $\Phi(\tilde{\boldsymbol{\sigma}}, \tilde{\boldsymbol{E}}) \leq 0$ and $\lambda \Phi(\tilde{\boldsymbol{\sigma}}, \tilde{\boldsymbol{E}}) = 0$. Inserting the time derivative of the thermodynamic potential (19) into the second law of thermodynamics leads, for the specific model problem (19) with (24), to the reduced dissipation inequality

$$\underbrace{-(\partial_{\boldsymbol{\varepsilon}^r} H_1 + \partial_{\boldsymbol{\varepsilon}^r} H_3)}_{\tilde{\boldsymbol{\sigma}}} : \dot{\boldsymbol{\varepsilon}}^r \underbrace{-(\partial_{\bar{N}^P} H_3 + \partial_{\bar{N}^P} H_4 + \partial_{\bar{N}^P} H_5)}_{\tilde{E}} \dot{\bar{N}}^P \geq 0 \,. \tag{29}$$

We reformulate (29) according to (15) in $\tilde{\boldsymbol{\sigma}} : \dot{\boldsymbol{\varepsilon}}^r + \tilde{E} \cdot \dot{\bar{N}}^P \geq 0$. Following [25] this expression is reduced to $\tilde{E} \cdot \dot{\bar{N}}^P \geq 0$ by using the constitutive relation

$$\boldsymbol{\varepsilon}^r = \frac{\varepsilon_a^r}{P_s^2} \operatorname{dev}(\boldsymbol{P}^r \otimes \boldsymbol{P}^r) \,, \tag{30}$$

where ε_a^r characterizes the maximum achievable remanent strain due to polarization in direction of the polarization axis. This quadratic relationship between the remanent polarization and strains is a commonly reasonable assumption, when the electric fields are strong and the stresses are small, see e.g. [20]. As a simple choice for the switching criterion we specify

$$\Phi = \tilde{E}^2 - E_c^2 \leq 0 \,, \tag{31}$$

with the coercive field strength E_c. The quantity $\tilde{E}$ is decomposed in $\tilde{E} = E - E^B$, with $E := -\partial_{\bar{N}^P} H_4 = J_2$ and the abbreviation

$$E^B := \partial_{\bar{N}^P} H_3 + \partial_{\bar{N}^P} H_5 \tag{32}$$

for the back electric field. Now the switching criterion appears in the explicit form

$$\Phi = (E - E^B)^2 - E_c^2 = (J_2 - E^B)^2 - E_c^2 \leq 0 \,. \tag{33}$$

For the numerical treatment we refer to [26, 28, 29]. As a numerical example we consider a quadratic plate with a centered hole, see Fig. 6. Here the microstructure is approximated by an ODF with 42 orientations per Gauß point. The applied electric voltage at the upper and lower edge is cycled from $\lambda = 0, 1, 0, -1 =: \{\lambda_0, \lambda_1, \lambda_2, \lambda_3\}$.

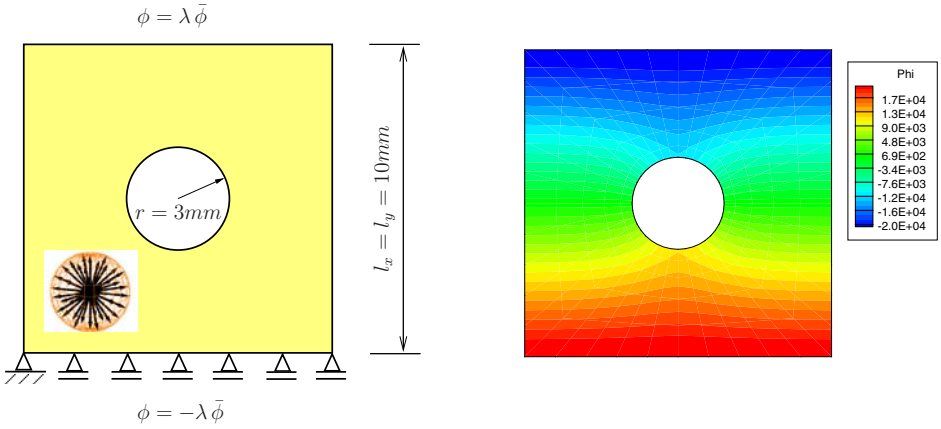

Fig. 6 (online colour at: www.gamm-mitteilungen.org) Left: Plate with a hole, discretized with 100 quadrilateral elements and 42 orientations per Gauß point. Right: Distribution of the electric potential at λ_1.

The material parameters are chosen close to $BaTiO_3$ at $\Theta = 25°C$: elasticity parameters $\lambda = 76.6 \cdot 10^9$, $\mu = 44.7 \cdot 10^9$, $\alpha_1 = -3.6 \cdot 10^9$, $\alpha_2 = 0.7 \cdot 10^9$, $\alpha_3 = 0.9 \cdot 10^9$, in $\mathrm{N/m^2}$, piezoelectric parameters $\beta_1 = 4.4$, $\beta_2 = 0.2$, $\beta_3 = -23.2$ in $\mathrm{C/m^2}$, dielectric parameters $\gamma_1 = -0.56 \cdot 10^{-8}$, $\gamma_2 = -0.07 \cdot 10^{-8}$ in $\mathrm{C/Vm}$, and $\varepsilon_a^r = 2.45 \cdot 10^{-4}$, $P_s = 26 \cdot 10^{-2}\mathrm{C/m^2}$. Fig. 7 depicts the distribution of the macroscopic polarization components P_1^r/P_s and P_2^r/P_s at three different loading stages.

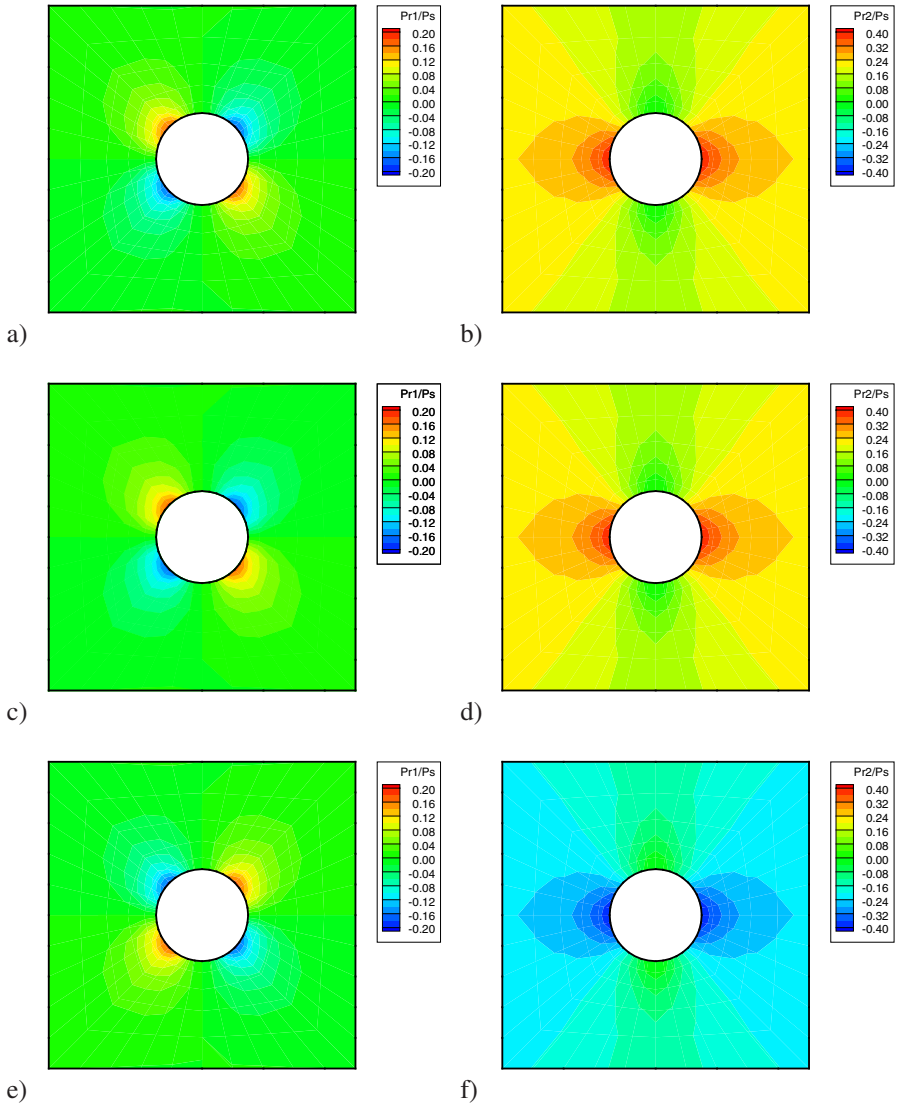

Fig. 7 (online colour at: www.gamm-mitteilungen.org) Distribution of the macroscopic remanent polarization. Left: P_1^r/P_s at a) λ_1, c) λ_2, e) λ_3. Right: P_2^r/P_s at b) λ_1, d) λ_2, f) λ_3.

5 Point defects

In a perfect crystal with an undisturbed lattice, all atoms are located at ideal lattice sites. On the continuum level, this is modelled as a homogeneous medium. Vacancies or foreign atoms lead to disturbance in the strain and charge state. On the continuum mechanics level, these defects can be modelled as a localized strain and as a localized charge. Thus for the

mechanical part the following assumption for the inelastic strain is made:

$$\boldsymbol{\varepsilon}^0 = \boldsymbol{\alpha}\,\delta(\boldsymbol{x}-\boldsymbol{\eta})\;, \tag{34}$$

where $\boldsymbol{\alpha}$ is the intensity of the defect and δ is the Dirac-delta distribution positioned at point $\boldsymbol{\eta}$. For simplicity it is often assumed, that the eigenstrain $\boldsymbol{\varepsilon}^0$ is isotropic, i.e. $\boldsymbol{\alpha} = \alpha\mathbf{1}$, but this assumption is very crude for complex crystals consisting of many different atom species. Nevertheless, we will assume an isotropic eigenstrain in the following. The material parameter α depends on the lattice structure and can be positive or negative. A positive sign represents a defect too large for its lattice site, a negative sign describes is a defect too small for the neighborhood or a vacancy.
Similarly, defect charges at a point $\boldsymbol{\eta}$ are modelled with a parameter β:

$$q = \beta\,\delta(\boldsymbol{x}-\boldsymbol{\eta})\;. \tag{35}$$

The determination of the defect parameters is a non-trivial task. Recently, comparison methods between atomistic and continuum mechanical simulations were used to identify these defect parameters. Details on a method based on the volumetric deformation induced by the defect can be found in [43, 44]. Here, the sign of β determines the sign of the charge of the defect.
Computing the gradient of the electric enthalpy $H(\boldsymbol{\varepsilon}-\boldsymbol{\varepsilon}^0, \boldsymbol{E}, \boldsymbol{P}^0)$ the balance law of configurational forces can easily be obtained by using the standard field equations. The result can be put in the format

$$\mathrm{div}\boldsymbol{\Sigma} + \boldsymbol{g} = \mathbf{0}\;, \tag{36}$$

where the $\boldsymbol{\Sigma}$ is the electro-mechanical Eshelby stress tensor, or configurational stress tensor and $\boldsymbol{g}$ is the configurational volume force. They are defined as

$$\boldsymbol{\Sigma} = H\mathbf{1} - (\nabla\boldsymbol{u})^{\mathrm{T}}\boldsymbol{\sigma} - \nabla\varphi\otimes\boldsymbol{D}\;, \tag{37}$$

$$\boldsymbol{g} = -(\nabla\boldsymbol{u})^{\mathrm{T}}\boldsymbol{f} + \nabla\varphi q + \boldsymbol{\sigma} : \nabla\boldsymbol{\varepsilon}^0 + (\nabla\boldsymbol{P}^0)^{\mathrm{T}}\boldsymbol{E} - \left.\frac{\partial H}{\partial\boldsymbol{x}}\right|_{\mathrm{expl.}}\;. \tag{38}$$

In the case of a homogeneous material with constant polarization $\boldsymbol{P}^0$ and in the absence of volume forces $\boldsymbol{f}$ the theory of material forces can be used to derive the driving force on a point defect:

$$\boldsymbol{G} = -\lim_{r\to 0}\int\limits_{V_{\boldsymbol{\eta}}(r)} \boldsymbol{g}\,dV \tag{39}$$

$$= -\lim_{r\to 0}\int\limits_{V_{\boldsymbol{\eta}}(r)} \left[\boldsymbol{\sigma} : \mathbf{1}\,\alpha\nabla\delta(\boldsymbol{x}-\boldsymbol{\eta}) + \nabla\varphi\beta\,\delta(\boldsymbol{x}-\boldsymbol{\eta})\right] dV \tag{40}$$

$$= -\left[-\alpha\nabla(\mathrm{tr}\boldsymbol{\sigma}) + \beta\nabla\varphi\right]\big|_{\boldsymbol{x}=\boldsymbol{\eta}} := \nabla\Lambda\big|_{\boldsymbol{x}=\boldsymbol{\eta}}\;, \tag{41}$$

see also [38, 39]. The field Λ is a force field on the defect in this electro-mechanical coupled system. The driving force due to the mechanical fields is given be the hydrostatic stress

state. Thus a center of expansion moves to regions where the lattice is already hydrostatically expanded and avoids regions of enhanced pressure. The second term in (41) represents the electrostatic force exerted on a point charge.
If defects are mobile and move with a velocity $\boldsymbol{v}$ in the lattice the dissipation due to defect motion can be written as

$$\mathcal{D}_{\mathrm{PD}} = \boldsymbol{G} \cdot \boldsymbol{v} \geq 0 \; . \tag{42}$$

Thus it is in agreement with the dissipation inequality to assume a kinetic relation of the form

$$\boldsymbol{v} = c_{\mathrm{PD}} \boldsymbol{G} \quad \text{with} \quad c_{\mathrm{PD}} \geq 0 \; . \tag{43}$$

An example of an isolated defect and two interacting defects in barium titanate is shown in Fig. 8. In order to compute the driving forces on a defect the field equations have to be solved. Fig. 8 shows the results for a computation using Fast Fourier Transform methods, see [38] for details on the numerical implementation. It is also possible to incorporate defects directly into Finite Element simulations. Details on this are given in [40]. Once the fields are solved the driving force field Λ can be obtained. The result for an arrangement with two defects is depicted in Fig. 8c). In addition, the driving forces acting on the defects are shown by two arrows. If defects are allowed to move according to the driving force by (43), they will follow the path shown in Fig. 8d), i.e. circling each other and finally approaching each other in the center of the simulation domain. The paths followed by defects are very complex and due to the anisotropy depend on the starting position of the two defects. For the system analysed here, almost all starting arrangements lead to a unification, only defects aligned with the principal axis of the material have the tendency to separate. For the interaction of more than two defects the reader is referred to [38].

6 Domain wall motion

To analyse the driving force on a single domain wall, the field equations of section 3 have to be supplemented by jump conditions on the domain wall. Within each domain, it is assumed that the spontaneous polarization $\boldsymbol{P}^0$ and the spontaneous strain ε^0 are constant, together with the material constants. The domain wall is treated as a sharp interface $\mathcal{S}$, which separates two domains $\mathcal{B}^+$ and $\mathcal{B}^-$. The normal vector $\boldsymbol{n}_{\mathcal{S}}$ on the interface $\mathcal{S}$ is pointing into domain $\mathcal{B}^+$. The balance laws on the interface reduce to the following jump relations

$$[\![\boldsymbol{\sigma}]\!] \boldsymbol{n}_{\mathcal{S}} = \boldsymbol{0} \quad \text{and} \quad [\![\boldsymbol{D}]\!] \cdot \boldsymbol{n}_{\mathcal{S}} = 0 \tag{44}$$

on the domain wall $\mathcal{S}$. Domain walls are perfectly bounded interfaces, thus the mechanical displacements $\boldsymbol{u}$ and the electric potential φ have to be continuous across the domain wall $\mathcal{S}$, i.e.

$$[\![\boldsymbol{u}]\!] = \boldsymbol{0} \quad \text{and} \quad [\![\varphi]\!] = 0 \; . \tag{45}$$

As a consequence of these assumptions the jump in rates can be written as

$$[\![\dot{\boldsymbol{u}}]\!] = -v_n [\![\nabla \boldsymbol{u}]\!] \boldsymbol{n}_{\mathcal{S}} \quad \text{and} \quad [\![\dot{\varphi}]\!] = -v_n [\![\nabla \varphi]\!] \cdot \boldsymbol{n}_{\mathcal{S}} \; , \tag{46}$$

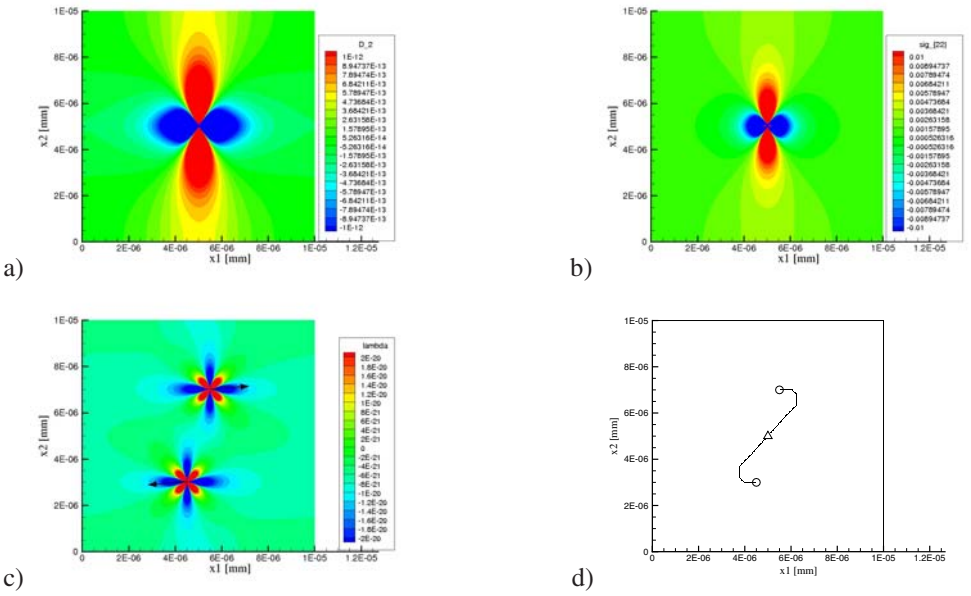

Fig. 8 (online colour at: www.gamm-mitteilungen.org) Point defects: a) isolated defect, electric displacement D_2, b) isolated defect, mechanical stress σ_{22}, c) two interacting defects, driving force and force field Λ at final position.

where v_n is the normal velocity of the domain wall. These jump conditions together with the equations in the bulk allow us to determine the driving force on a domain wall. Details on this derivation are omitted here for the sake of brevity. Details can be found in [41]. In [40] also a variational setting is discussed. In addition to the bulk energy, i.e. the electric enthalpy H, an isotropic and constant interface energy density γ is assumed for the domain wall. Thus the total energy of the system is comprised of

$$E = \int_{\mathcal{B}} H \, dV + \gamma \int_{\mathcal{S}} dA \, . \tag{47}$$

Again utilizing the theory of material or configurational forces, the driving force on a domain wall can be computed. As a result the force τ_n per unit area of domain wall is given as

$$\tau_n = \boldsymbol{n}_{\mathcal{S}} \cdot (\llbracket \boldsymbol{\Sigma} \rrbracket \boldsymbol{n}_{\mathcal{S}}) + \gamma \kappa \tag{48}$$

where κ is twice the mean curvature. The Eshelby stress tensor takes the changes of the electric enthalpy and the work done by the fields into account as a domain wall moves through the lattice. The curvature term is related to the creation or annihilation of interface area due to domain wall motion. Thus except for simple cases the simulation of domain wall motion requires the solution of the entire coupled field problem, taking spontaneous strain and polarization into account. If the domain wall moves with a velocity v_n in normal direction through the lattice the dissipation due to this process is given by

$$\mathcal{D}_{\mathcal{S}} = \tau_n v_n \geq 0 \, . \tag{49}$$

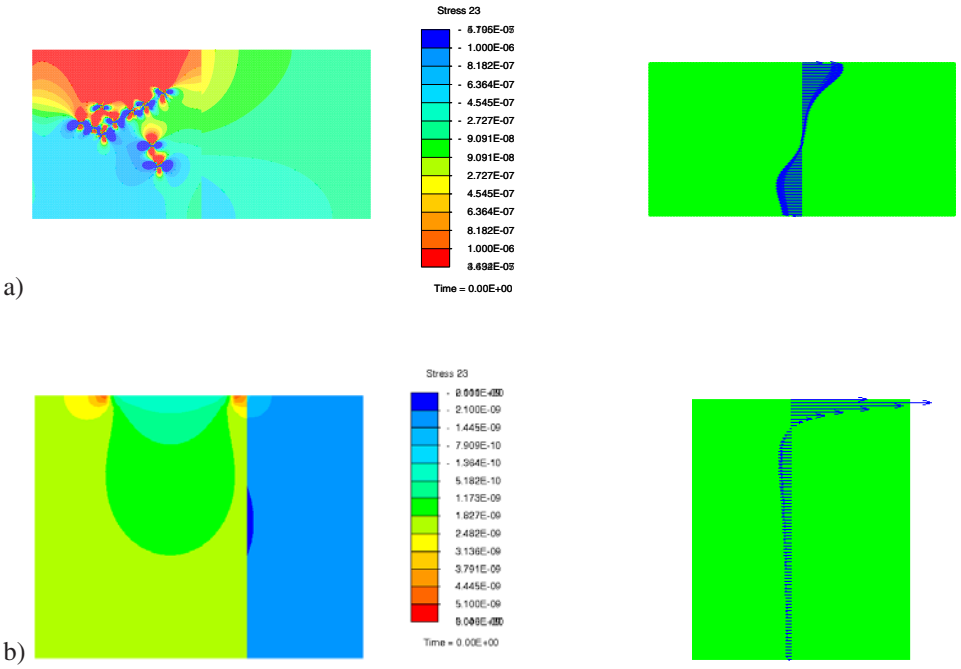

Fig. 9 (online colour at: www.gamm-mitteilungen.org) Electric displacement and driving force on a 180° domain wall in conjunction with defects: a) point defects, b) surface (electrode) defect.

Note, that the tangential velocity is no intrinsic quantity and thus cannot have an influence on the dissipation. Again the dissipation inequality can be used to postulate a kinetic relation. Based on experimental observations for single crystal systems [42] the following kinetic relation was proposed

$$v_n = c_{\mathcal{S}} \langle |\tau_n| - \tau_0 \rangle \, \mathrm{sign} \tau_n \ , \tag{50}$$

which resembles a visco-plastic law of Perzyna type. For the domain wall to move, a threshold value τ_0 has to be overcome. Once this threshold value is exceed the domain wall moves with a velocity v_n proportional to the overload $|\tau_n| - \tau_0$. The mobility coefficient of this motion is $c_{\mathcal{S}} > 0$. The kinetic coefficients $c_{\mathcal{S}}$ and τ_0 were determined by experiment on single crystals with planar domain walls, where the interface energy terms can be neglected. Details on this procedure can be found in [41].

The presence of defects, which may be point or surface defects, perturb the local fields at the domain wall and lead to an inhomogeneous distribution of the driving force on the domain wall. Such situations are shown in Fig. 9 for different defects. It can be seen that compared to the defect free state the overall driving force on a 180° domain wall is reduced, which

demonstrates that the presence of defects diminish the motion of domain walls. Their presence and arrangement in the material is therefore related to fatigue phenomena. Especially, if the defects are mobile themselves their redistribution can reduce domain wall motion, resulting in macroscopic fatigue, i.e. deformation of the electric hysteresis loops and butterfly loops. The details of these complex interaction processes are still not fully understood. More results can be found in [40].

7 Final remarks

The complexity of the ferroelectric material behavior has to be modelled at different length scales. A macroscopic model has to not only be thermodynamic consistent but also has to take the key properties of the microstructure into account. The presented model of an orientation distribution function serves this purpose very well. In order to understand the effects associated with fatigue the details of domain wall motion and defect interaction have to considered. The models for domain wall motion and defect migration are also thermodynamic consistent and explain the formation of defect clusters and the pining of domain walls by such clusters. Future work should consider the microscopic details of the fatigue mechanisms, which are also experimentally observed, in order to develop a macroscopic model with appropriate internal variables.

References

[1] D. C. Lupascu and M. Hammer, Elastic Discontinuities during Switching of Ferroelectric Ceramics, phys. stat. sol. (a) **191**, No. 2, 643-657 (2002).
[2] H. Aburatani and K. Uchino, Acoustic emission (AE) measurement technique in piezoelectric ceramics, Jpn. J. Appl. Phys. Part 2-Lett. **35**, No. 4B, L516–L518 (1996).
[3] A. G. Chynoweth, Barkhausen pulses in barium titanate, Phys. Rev. **110**, No. 6, 1316–1332 (1958).
[4] C. A. Randall, N. Kim, J.-P. Kucera, W. Cao, and T. R. Shrout, Intrinsic and extrinsic Size Effects in Fine-Grained Morphotropic-Phase-Boundary Lead Zrconate Titanate Ceramics, J. Am. Ceram. Soc. **81**, No. 3, 677–688 (1998).
[5] M. Vollmann, R. Hagenbeck, and R. Waser, Grain- Boundary Defect Chemistry of Acceptor-Doped Titanates: Inversion Layer and Low- Field Conduction, J. Am. Ceram. Soc. **80**, No. 9, 2301–2314 (1997).
[6] G. Arlt, H. Neumann, Internal Bias in Ferroelectric Ceramics: Origin and Time Dependence, Ferroelectrics **87**, 109–120 (1988).
[7] Y. A. Genenko and D. C. Lupascu, Drift of charged defects in local fields as aging mechanism in ferroelectrics, Phys. Rev. B **75**, 184107 (2007).
[8] J. F. Scott and M. Dawber, Oxygen-vacancy ordering as a fatigue mechanism in perovskite ferroelectrics, Appl. Phys. Lett. **76**, No. 25, 3801–3803 (2000).
[9] L. Pintilie and M. Alexe, Metal-ferroelectric-metal heterostructures with Schottky contacts. I. Influence of the ferroelectric properties, J. Appl. Phys. **98**, 124103 (2005).
[10] J. F. Scott and F. M. Ross, New results on layer-structure perovskite ferroelectric thin-film memories, Ferroelectrics **201**, 43–53 (1997).
[11] T. Mihara, H. Watanabe, H. Yoshimori, C. A. Paz De Araujo, B. Melnick, and L. D. McMillan, Process dependent electrical characteristics and equivalent circuit model of sol-gel based PZT capacitors, Integr. Ferroelec. **1**, 269–291 (1992).
[12] D. C. Lupascu and J. Rödel, Fatigue in Bulk Lead Zirconate Titanate Actuator Materials, Adv. Engin. Mater. **7**, No. 10, 882–898 (2005).
[13] D. C. Lupascu, Fatgue in ferroelectric ceramics and related issues, (Springer, Heidelberg, 2004).
[14] C. S. Lynch, The effect of uniaxial stress on the electro-mechanical response of 8/65/35 PLZT, Acta mater. **44**, No. 10, 4137–4148 (1996).
[15] J. Nuffer, D. C. Lupascu, and J. Rödel, Damage evolution in ferroelectric PZT induced by bipolar electric cycling, Acata Mater. **48**, 3783-3794 (2000).
[16] D. C. Lupascu, S. Fedosov, C. Verdier, J. Rödel, and H. von Seggern, Stretched exponential relaxation in perovskite ferroelectrics after cyclic loading, J. Appl. Phys. **95**, No. 3, 1386–1390 (2004).
[17] W. Diffie and E. Hellman, New directions in cryptography, IEEE Transactions on Information Theory **22**, No. 5, 644–654 (1976).
[18] J.P. Boehler, Applications of Tensor Functions in Solid Mechanics, CISM Course No. 292 (Springer, Heidelberg, 1987).
[19] R. Hill, Journal of the Mechanics and Physics of Solids **11**, 357–372 (1963).
[20] B. Jaffe et al., Piezoelectric Ceramics (Academic Press, London, New York, 1971).
[21] C.M. Landis, Journal of the Mechanics and Physics of Solids **50**, 127–152 (2002).
[22] J. Lemaitre and J.-L. Chaboche, Mechanics of solid materials, Cambridge University Press, Cambridge (1990).
[23] I. Liu, International Journal of Engineering Science **20**, 1099–1109 (1982).
[24] D.G. Luenberger, Linear and Nonlinear Programming, Addison-Wesley, Massachusetts (1984).
[25] R.M. McMeeking and C.M. Landis, International Journal of Engineering Science **40**, 1553–1577 (2002).
[26] H. Romanowski, Kontinuumsmechanische Modellierung ferroelektrischer Materialien im Rahmen der Invariantentheorie, Promotionsschrift, Universität Duisburg-Essen, Bauwissenschaften, Institut für Mechanik, (2006).

[27] I. Kurzhöfer, Mehrskalen-Modellierung polykristalliner Ferroelektrika basierend auf diskreten Orientierungsverteilungsfunktionen, Promotionsschrift, Universität Duisburg-Essen, Bauwissenschaften, Institut für Mechanik, (2007).
[28] H. Romanowski and J. Schröder, Coordinate invariant modelling of the ferroelectric hysteresis within a thermodynamically consistent framework. A mesoscopic approach, In: Trends in Applications of Mathematics to Mechanics, Eds. Y. Wang, K. Hutter, 419-428 (2005).
[29] J. Schröder and H. Romanowski, Archive of Applied Mechanics **74**, 863–877 (2005).
[30] J. Schröder, H. Romanowski and I. Kurzhöfer, Meso-Macro-Modeling of Nonlinear Ferroelectric Ceramics, Online Proceedings of the 5th International Conference on Computation of Shell and Spatial Structures, Eds.: E. Ramm, W.A. Wall, K. Bletzinger and M. Bischoff; June 1-4, 2005, Salzburg, Austria.
[31] J. Schröder and D. Gross, Archive of Applied Mechanics **73**, 533–552 (2004).
[32] G.F. Smith, Archive of Rational Mechanics and Analysis **36**, 161–165 (1970).
[33] G.F. Smith, International Journal of Engineering Science **19**, 899–916 (1971).
[34] A.J.M. Spencer, Theory of Invariants in A.C. Eringen (ed.): Continuum Physics Vol. 1 (Academic Press, New York, 1971).
[35] A.J.M. Spencer, Applications of Tensor Functions in Solid Mechanics, CISM Course No. 282 (Springer, Heidelberg, 1987).
[36] C.C. Wang, Archive of Rational Mechanics and Analysis **33**, 249–267 (1969).
[37] C.C. Wang, Archive of Rational Mechanics and Analysis **33**, 268–287 (1969).
[38] O. Goy, R. Müller, D. Gross, Interaction of point defects in piezoelectric materials numerical simulations in the context of electric fatigue, J. Thero. Appl. Mech., **44**, No. 4, 819–836 (2006).
[39] D. Gross, S. Kolling, R. Müller, I. Schmidt, Configurational Forces and their Application in Solid Mechanics, Europ. J. Mech./A Solids, **22**, 669–692 (2003).
[40] R. Müller, D. Gross, D. C. Lupascu, Driving forces on domain walls in ferroelectric materials and interaction with defects, Comp. Mat. Sci., **35**, 42–52 (2006).
[41] D. Schrade, R. Müller, D. Gross, T. Utschig, V. Y. Shur, D. C. Lupascu, Interaction of domain walls with defects in ferroelectric materials, Mechanics of Materials, **39**, No. 2, 161–174 (2006).
[42] R. Flippen, Domain wall dynamics in ferroelectric/ ferroelastic molybdates, J. Appl. Phys. **46**, No. 3, 1068–1071 (1975).
[43] K. Garikipati, M. Falk, M. Bouville, B. Puchala, H. Narayanan, The continuum elastic and atomistic viewpoints on the formation volume and strain energy of a point defect, J. Mech. Phys. Solids, **54**, No. 9, 1929–1951 (2006).
[44] O. Goy, R. Müller, D. Gross, Modelling of Point Defects in anisotropic media with an application to Ferroelectrics, Comp. Mat. Sci., submitted (2007).

